Supplementary Information (SI) for Catalysis Science & Technology.

Supporting Information - Tailored support reduction of $Cu/SrTiO_3$ catalysts for enhanced methanol production

C. Pischetola[a,*], L. Artiglia[a], F. Krumeich[b] and J. A. van Bokhoven[a,b*]

a. Paul Scherrer Institute, Center for Energy and Environmental Sciences, Forschungsstrasse 111, 5232, Villigen, Switzerland
b. Institute for Chemical and Bioengineering, ETH Zurich, Vladimir-Prelog-Weg 1, 8093, Zurich, Switzerland

* Email: chiara.pischetola@psi.ch
* Email: jeroen.vanbokhoven@chem.ethz.ch

Catalyst Performance Indicators

The carbon dioxide conversion (X_{CO2}, %) was calculated as:

$$X_{CO2} = \frac{C_{CO2}^{in} - C_{CO2}^{out}}{C_{CO2}^{in}} \times 100 \qquad \text{S1}$$

where C_{CO2} is the carbon dioxide concentration in input (in) or output (out) from the reactor.

The methanol selectivity (S_{MeOH}, %) is defined as:

$$S_{MeOH} = \frac{\dot{n}_{MeOH}}{(\dot{n}_{MeOH} + \dot{n}_{CO})} \times 100 \qquad \text{S2}$$

where $\dot{n}_i$ is the molar flow of chemical i (mmol min^{-1}), determined as:

$$\dot{n}_i = C_i^{out} * flow_{tot}^{out} \qquad \text{S3}$$

The methanol space time yield (STY, $g_{MeOH}\ g_{cat}^{-1}\ h^{-1}$) is given as

$$STY = \frac{\dot{n}_{CO2}^{in} * (\chi_{CO2}/100) * (S_{MeOH}/100) * MW_{MeOH}}{m_{catlyst}} \times 60 \qquad \text{S4}$$

where MW_{MeOH} is methanol molecular weight and $m_{catalyst}$ is the total mass of Cu/STO catalyst.

Table S1. Chemical properties and red-ox characterisation from H_2-TPR experiments of copper-supported catalyst on commercial $SrTiO_3$.

Material	Name	Cu content (wt. %)[a]	H_2-TPR experiments	
			Reduction T (°C)	Hydrogen consumed (mmol g_{cat}^{-1})
$SrTiO_3$	STO_C	0	-	0
$Cu/SrTiO_3$	2_STO_C	2.7	190	0.41

a = from ICP measurements.

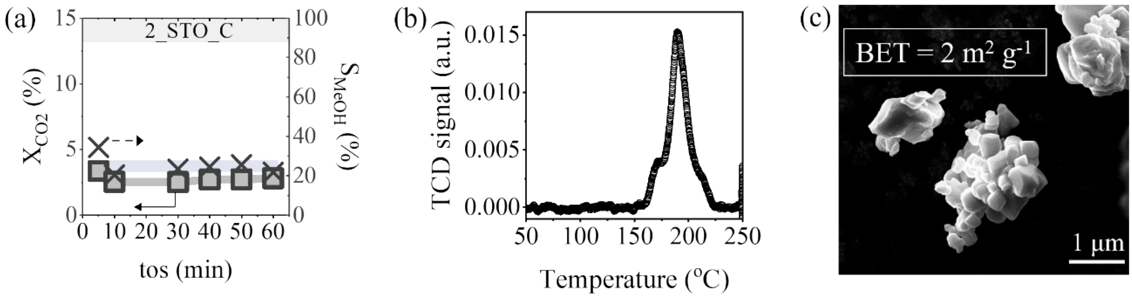

Figure S1. (a) Time on stream (tos, min) profiles of carbon dioxide conversion (X_{CO2}, %) and methanol selectivity (S_{MeOH}, %) over 2_STO_C. **(b)** H_2-TPR profile at 1 bar of 2_STO_C. **(c)** SEM image of as-received STO_C, with associated BET surface area.

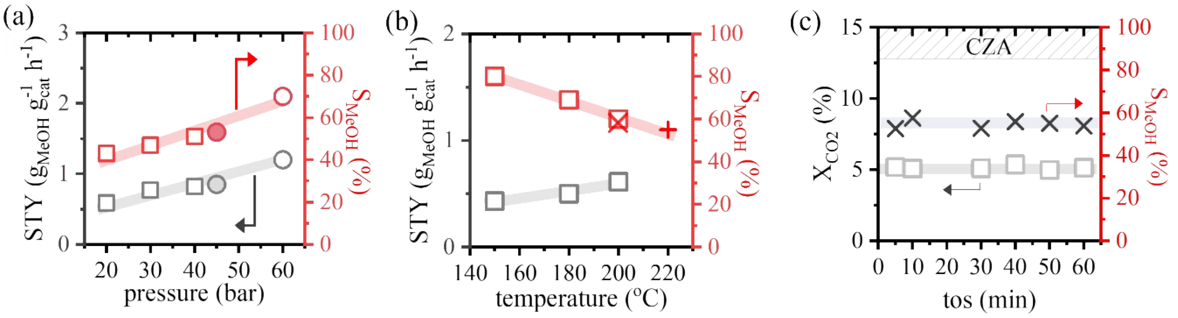

Figure S2. (a) Pressure-dependence and **(b)** temperature-dependence performance (*i.e.* STY (g_{MeOH} g_{cat}^{-1} h^{-1}, grey symbols) and S_{MeOH} (%, red symbols)) of CZA in carbon dioxide hydrogenation over the fixed-bed reactor of this study (square) and set-ups from literature (circle: open,[1] solid;[2] X,[3] and +[4]). **(c)** Time on stream (tos, min) profiles of carbon dioxide conversion (X_{CO2}, %) and methanol selectivity (S_{MeOH}, %) over CZA. Reaction conditions: in **(a)** $T = 250$ °C, in **(b)** $p = 30$ bar, in **(c)** $p = 30$ bar, T = 200 °C; GHSV 21600-28000 h^{-1}.

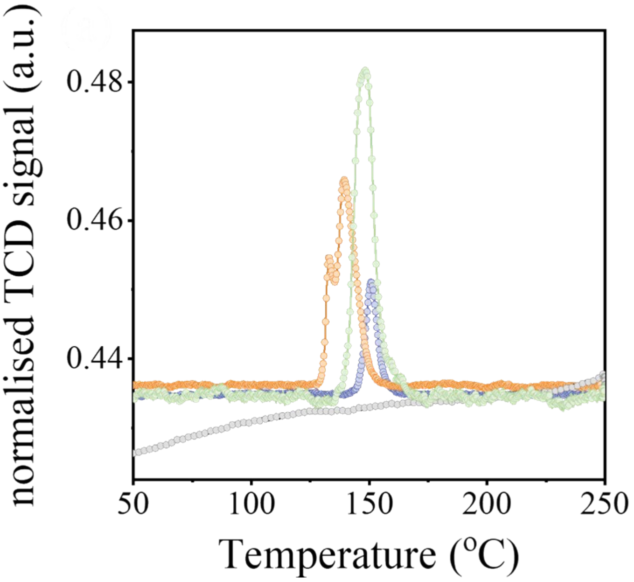

Figure S3. Mass-normalised H_2-TPR profiles of bare STO (100 mg_{cat}, grey), 1_STO (51 mg_{cat}, violet), 2_STO (70 mg_{cat}, orange) and 5_STO (12 mg_{cat}, green)

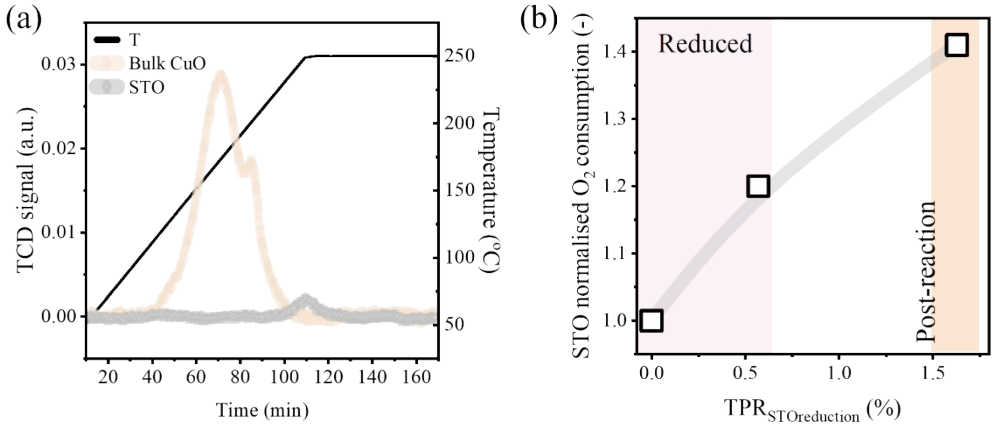

Figure S4. (a) O_2-TPO profile at 1 bar of bulk CuO (pink) and bare STO (grey). **(b)** Correlation of normalized (with respect to bare STO) O_2 consumption from O_2-TPO of fresh 2_STO and *post*-reaction HP2_STO with STO reduction degree from H_2-TPR. *Note:* only the high-temperature TPO peak is considered.

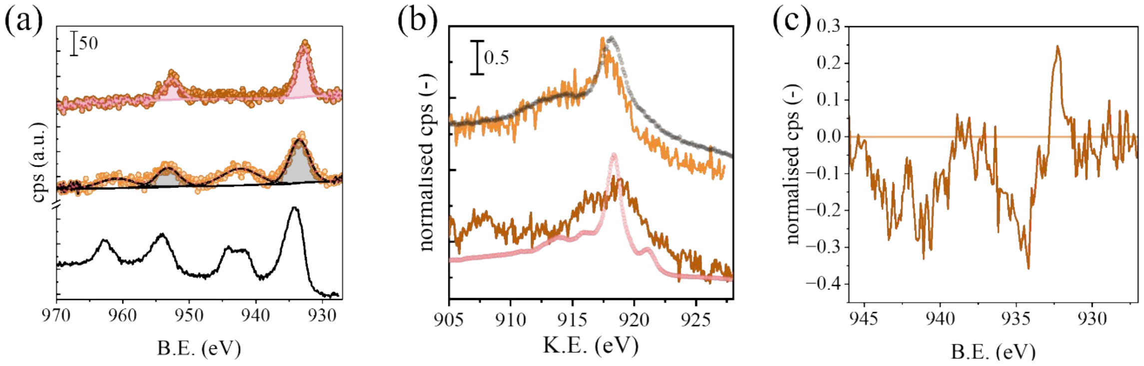

Figure S5. (a) Deconvolution of Cu 2p photoemission spectra of 2_STO (light orange) and *post*-reaction HP2_STO (dark orange). The experimental data are given as solid circles. The fitting of CuO and Cu(0)/Cu(I) components is given by black and pink areas, respectively, while the envelope is a dotted red line. Standard CuO spectrum is reproduced in solid black line. **(b)** Cu LMM Auger lines of 2_STO and *post*-reaction HP2_STO in kinetic energy (K.E.) scale; superimposed dotted black and pink scatters are reference spectra of CuO nanoparticles (in-house measured) and bulk metallic Cu foil (from ref [5]), respectively. **(c)** Area-normalized Cu 2p profile of *post*-reaction HP2_STO (dark orange) subtracted from that of fresh 2_STO (light orange).

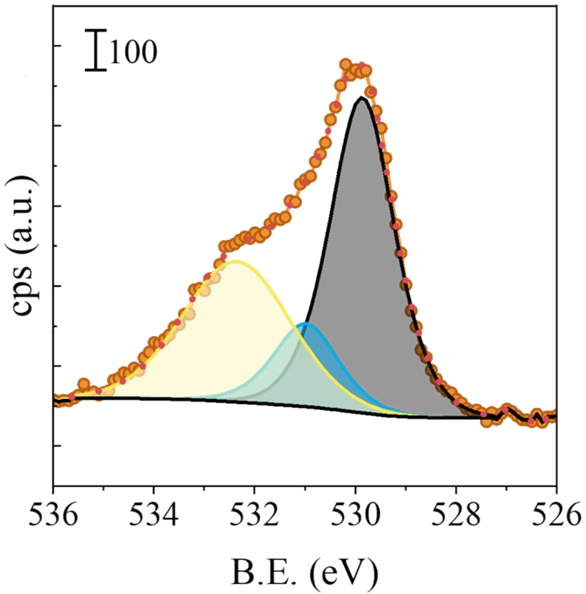

Figure S6. Deconvolution of O 1s photoemission spectrum of HP2_STO. The experimental data are given as solid circles, while the envelope is a dotted red line. The fitting of the following components (i) lattice oxygen of $SrTiO_3$, (ii) the oxygen adjacent to OVs and (iii) the chemisorbed oxygen is represented by black, blue and yellow areas, respectively.

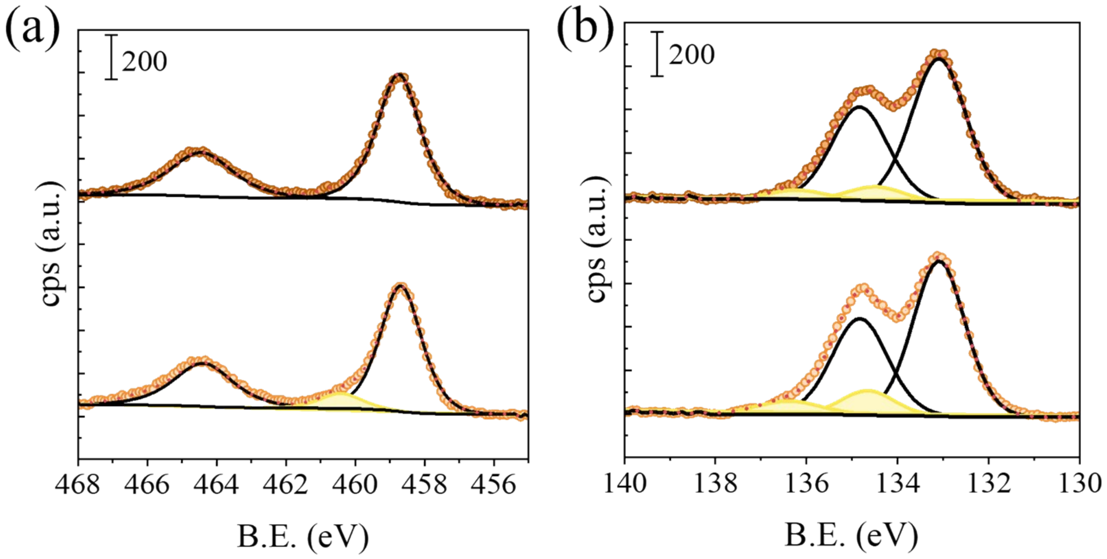

Figure S7. Deconvolution of **(a)** Ti 2p and **(b)** Sr 3d photoemission spectra of 2_STO (light orange) and HP2_STO (dark orange). The experimental data are given as solid circles. The fitting of main peak and extra features are black and yellow lines, respectively. The envelope is a dotted red line.

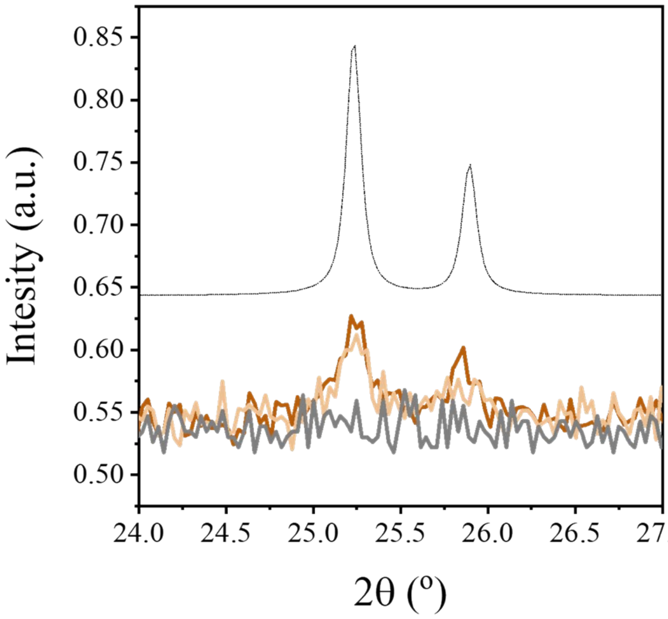

Figure S8. XRD patterns of STO (grey), 2_STO (light orange) and HP2_STO *post*-reaction (dark orange). Standard $SrCO_3$ is reproduced as black dotted line.

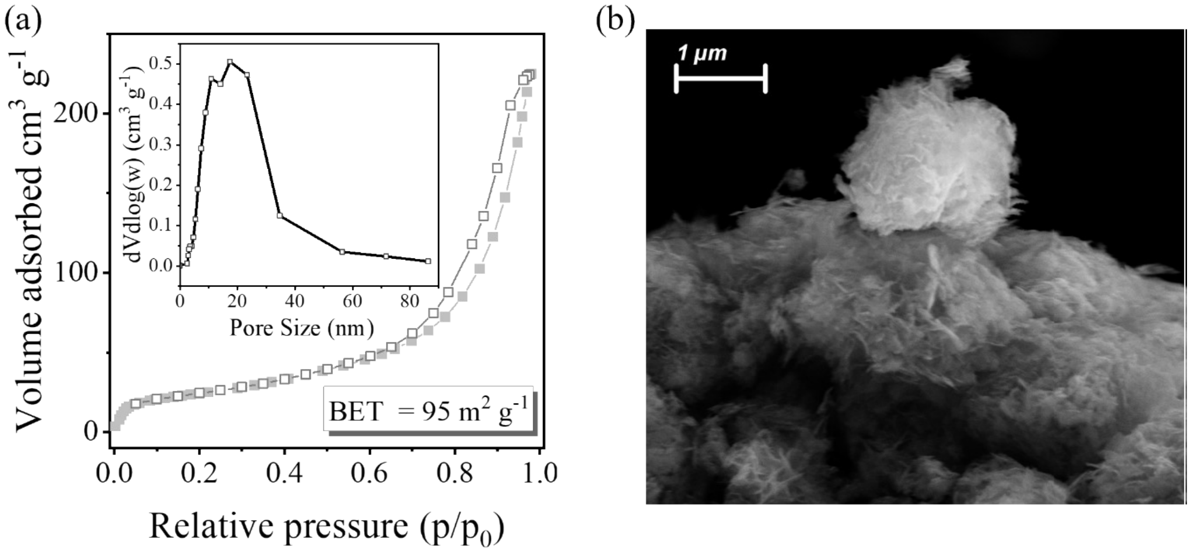

Figure S9. (a) N_2-physisorption measurement and pore size distribution (as insert) of STO. The full and open grey squares represent the adsorption and desorption branches, respectively. **(b)** SEM image of as-synthesised STO.

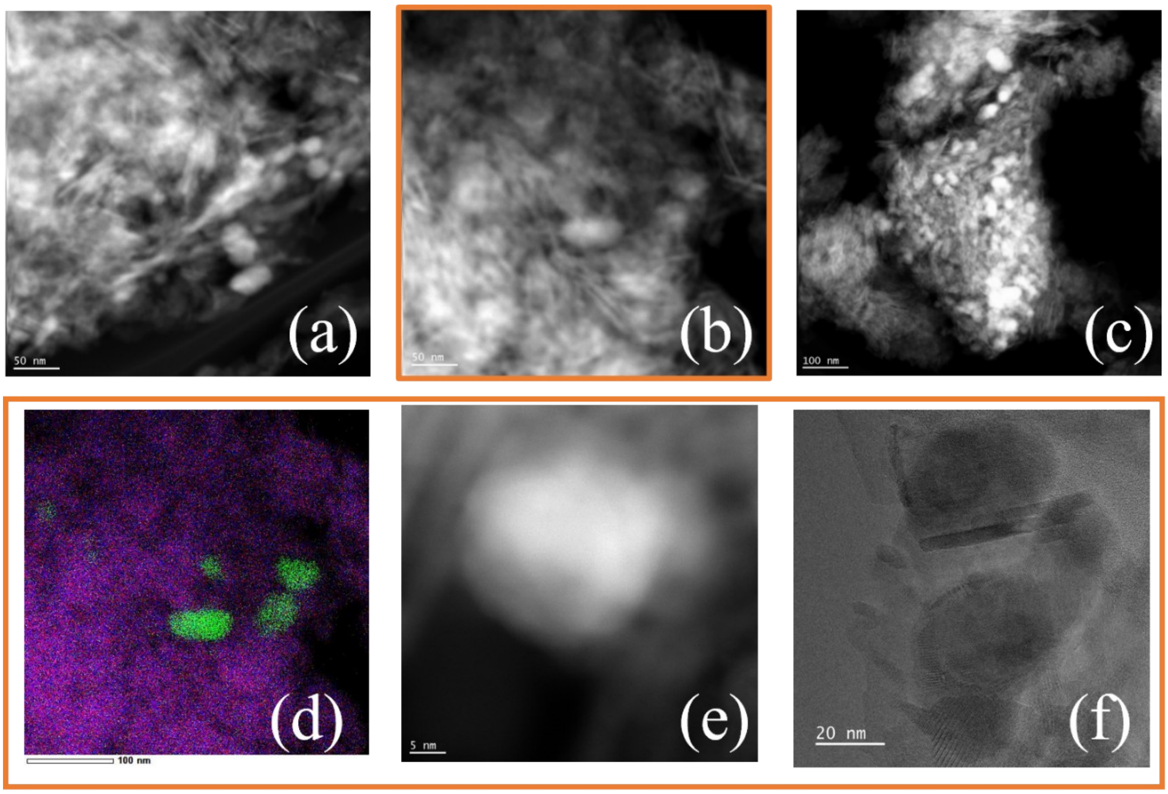

Figure S10. **(a)-(c)** HAADF-STEM pictures of 1_STO, 2_STO and 5_STO *post*- H_2-TPR at 1 bar, respectively. Images in the orange box refer to 2_STO: **(d)** EDX mapping associated to **(b)** where green areas represent counts from copper species on Ti + Sr + O overlay is given in purple. **(e)** High magnification STEM and **(f)** HRTEM.

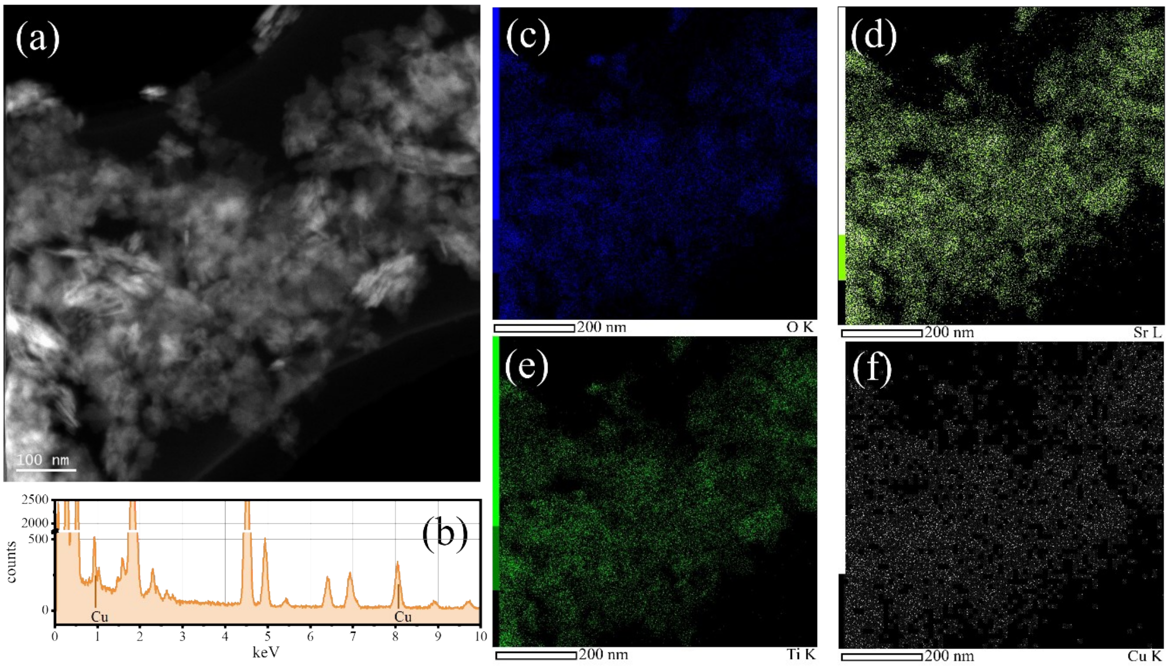

Figure S11. (a) HAADF-STEM of 2_STO *post*-H_2-TPR with associated **(b)** EDX spectrum and **(c)**-**(f)** elemental mapping of O (blue), Sr (yellow), Ti (green) and Cu (white), respectively.

Table S2. Fitting parameters and computed data from the deconvolution of the Cu 2p, Ti 2p and Sr 3d photoemission core level of STO, 2_STO and HP2_STO *post*-reaction (PR).

Catalyst		B.E. (eV)	Splitting (eV)	Fitting Function	FWHM (eV)	Concentration (%)
STO	Cu 2p3/2	-	-	-	-	-
	Ti 2p3/2	458.7	5.7	GL(80)	1.2	100
	Sr 3d5/2	133.3	1.7	GL(30	1.5	100
2_STO	Cu 2p3/2	933.5	19.8	GL(30)	3.3	100
	Ti 2p3/2	458.7	5.7	GL(60)	1.4	89.3
		460.4	5.7	GL(60)	1.4	10.7
	Sr 3d5/2	133.1	1.7	GL(30	1.4	86.3
		134.6	1.7	GL(30	1.4	13.7
HP2_STO PR	Cu 2p3/2	932.8	19.8	GL(30)	2.5	100
	Ti 2p3/2	458.7	5.7	GL(70)	1.5	100
	Sr 3d5/2	133.1	1.7	GL(30)	1.4	91.0
		134.5	1.7	GL(30)	1.4	9.0

Table S3. Fitting parameters and computed data from the deconvolution of the O 1s photoemission core level of STO, 2_STO and HP2_STO *post*-reaction (PR).

Catalyst		B.E. (eV)	Fitting Function	FWHM (eV)	Concentration (%)
STO	O1s	529	-	-	0
		530.1	GL(60)	1.7	77.5
		531	-	-	0
		531.8	GL(70)	2.0	22.5
2_STO	O1s	529.1	GL(80)	1.0	15.2
		529.6	GL(70)	1.7	49.0
		531.0	-	-	0
		531.6	GL(70)	2.5	35.8
HP2_STO PR	O1s	529.0	-	-	0
		529.8	GL(70)	1.5	47.5
		530.9	GL(70)	1.5	14.1
		532.3	GL(70)	2.5	38.4

XPS Data Analysis

Cu analysis. The main photoemission peak ($2p_{3/2}$) of 2_STO is fitted with a single component centred at 933.5 eV (see **Figure S5(a)**) with associated shake-up satellites between 940 and 946 eV [6] and the spin orbit satellite $2p_{1/2}$ peak is found at 953.3 eV with shake-up satellites between 959.0 and 966.0 eV [7].

Concerning HP2_STO, the curve deconvolution is performed by fitting one peak centred at 932.8 eV. Because Cu^+ and Cu^0 species display similar B.E. values, this component can be assigned to one of these oxidation states.[8] The analysis of the Auger $CuL_3M_{4.5}M_{4.5}$ spectrum (**Figure S5(b)**) is of critical importance to be able discriminating between them.[5,9] The centroid of the main peak overlaps with that of metallic copper, but the shape differs from the reference, probably due to the presence of Cu(I) as a consequence of partial Cu nanoparticles reoxidation during sample transfer in air from the reaction to the XPS setup.

O analysis. The O 1s signal of STO in **Figure 4(c)** presents an asymmetric shape resulting from the combination of the main feature (77.6%) at 530.1 eV, attributed to lattice oxygen in O-Metal bonds,[10,11] with a shoulder (22.5%) at higher B.E. ($\Delta = +1.6$ eV) that can be assigned to O-containing species adsorbed on the surface.[12,13] Clear changes in the O 1s spectra of 2_STO and HP2_STO are observed; namely, the main peak shifts negatively (fresh catalyst >> *post*-reaction) and a shoulder develops at B.E. >530.5 eV. Four regions are highlighted in the inset of **Figure 4(c)**, where positive signals are indicative of new spectral features appearing, and *vice versa*. The first region, going from lower to higher B.E., displays a positive feature present only in 2_STO and centred at 529.12 eV. The grey shaded spectral region contains negative peaks observed for both 2_STO and HP2_STO suggesting a relative decrease of the $SrTiO_3$ (lattice oxygen) component.[14,15] Another feature at B.E. = 530.9 eV (blue spectral region) is present only for HP2_STO (estimated fraction of 14.1%, see **Table S3**). The last spectral region at high B.E. (yellow) is characterised by positive contributions observed on both catalysts and contains peaks centred at 531.7 and 532.3 eV, respectively.

Ti analysis. No significant change in peak position/shape is observed for the Ti $2p_{3/2}$ (B.E. = 458.7 eV) and Ti $2p_{1/2}$ (B.E. = 464.42±0.02 eV) doublet of the three materials; the values agree with those of Ti^{4+}.[10]

Sr analysis. The Sr 3d signal of STO presents a doublet with peaks located at 133.28 and 135.02 eV, attributed to the $3d_{5/2}$ and $3d_{3/2}$ contributions of Sr^{2+}, respectively.[16] 2_STO and HP2_STO require a new doublet, shifted by approx. 1.4 eV from the main one of STO, to obtain a good correlation, as shown in the deconvolution of **Figure S7(b)**). On HP2_STO, the concentration of this second feature decreases from 13.7 to 9 %.

References

1 H. Ruland, H. Song, D. Laudenschleger, S. Stürmer, S. Schmidt, J. He, K. Kähler, M. Muhler and R. Schlögl, *ChemCatChem*, 2020, **12**, 3216–3222.

2 B. Hu, Y. Yin, Z. Zhong, D. Wu, G. Liu and X. Hong, *Catalysis Science & Technology*, 2019, **9**, 2673–2681.
3 S. Kanuri, S. Dinda, S. A. Singh, S. Roy, C. Chakraborty and S. P. Datta, *Materials Today Chemistry*, 2024, **36**, 101959.
4 H. Li, L. Wang, X. Gao and F.-S. Xiao, *Ind. Eng. Chem. Res.*, 2022, **61**, 10446–10454.
5 M. C. Biesinger, *Surface and Interface Analysis*, 2017, **49**, 1325–1334.
6 F. Parmigiani and L. Sangaletti, *Journal of Electron Spectroscopy and Related Phenomena*, 1994, **66**, 223–239.
7 M. C. Biesinger, *Surface & Interface Analysis*, 2017, **49**, 1325–1334.
8 J. P. Espinós, J. Morales, A. Barranco, A. Caballero, J. P. Holgado and A. R. González-Elipe, *The Journal of Physical Chemistry B*, 2002, **106**, 6921–6929.
9 G. Moretti and P. Porta, *Journal of Physics: Condensed Matter*, 1989, **1**, SB193.
10 K. Aravinthkumar, E. Praveen, A. J. R. Mary and C. R. Mohan, *Inorganic Chemistry Communications*, 2022, **140**, 109451.
11 M. C. Biesinger, L. W. Lau, A. R. Gerson and R. S. C. Smart, *Applied surface science*, 2010, **257**, 887–898.
12 Y. Zhu, L. Zhang, B. Zhao, H. Chen, X. Liu, R. Zhao, X. Wang, J. Liu, Y. Chen and M. Liu, *Advanced Functional Materials*, 2019, **29**, 1901783.
13 Y. Lu, A. Ma, Y. Yu, R. Tan, C. Liu, P. Zhang, D. Liu and J. Gui, *ACS Sustainable Chemistry & Engineering*, 2018, **7**, 2906–2910.
14 M. Humayun, L. Xu, L. Zhou, Z. Zheng, Q. Fu and W. Luo, *Nano Research*, 2018, **11**, 6391–6404.
15 L. Fu, J. Zhou, J. Yang, Q. Li, H. Guo, Q. Deng, Z. Zhu, Z. Zhang, H. Yu and K. Wu, *Applied Surface Science*, 2022, **592**, 153269.
16 P. A. W. Van der Heide, Q. D. Jiang, Y. S. Kim and J. W. Rabalais, *Surface Science*, 2001, **473**, 59–70.